Theoretical and Numerical Study of Wave Port Boundary Conditions for Lorenz Gauge Potential-Based Finite Element Methods

Thomas E. Roth[*] and Colin A. Braun

Abstract—The development of computational electromagnetics methods using potential-based formulations in the Lorenz gauge have been gaining interest as a way to overcome the persistent challenge of low-frequency breakdowns in traditional field-based formulations. Lorenz gauge potential-based finite element methods (FEM) have begun to be explored, but to date have only considered very simple excitations and boundary conditions. In this work, we present a theoretical and numerical study of how the widely used wave port boundary condition can be incorporated into these Lorenz gauge potential-based FEM solvers. In the course of this, we propose a new potential-based FEM approach for analyzing inhomogeneous waveguides that is in the same gauge as the 3D potential-based methods of interest to aid in verifying theoretical claims. We find that this approach has certain null spaces that are unique to the 2D setting it is formulated within that prevent it from overcoming low-frequency breakdown effects in practical applications. However, this method still is valuable for presenting numerical validation of other theoretical predictions made in this work; particularly, that any wave port boundary condition previously developed for field-based methods can be utilized within a 3D Lorenz gauge potential-based FEM solver.

1. INTRODUCTION

Analyzing inhomogeneous waveguides to determine their modal propagation constants and field distributions has a long history in the design of microwave and optical components [1–13], with the finite element method (FEM) the most popular numerical method used for solving these problems [14]. In these methods, Maxwell's equations are recast into a suitable eigenvalue problem in the waveguiding geometry to determine the modal properties. Although these solutions are useful in their own right, they also form the foundation of implementing wave port boundary conditions in a full 3D FEM analysis [14, 15]. Wave port boundary conditions are the most accurate excitation and termination for waveguiding problems in a 3D FEM analysis, and so form an essential component in a general-purpose FEM analysis suite.

Unfortunately, the low-frequency breakdown that is inherent to traditional field-based FEM solvers continues to be a problem for these methods. These breakdowns occur when parts of the geometry being analyzed are significantly smaller than the wavelength being considered [8, 9, 14, 16], which can be especially prevalent in the analysis of digital or mixed-signal integrated circuits [6, 7]. To tackle the modeling challenges of these applications, it is necessary to have a robust numerical method that can seamlessly model problems over a wide range of frequencies and length scales, ideally without resorting to specialized fixes that only work in specific scenarios.

Potential-based methods are gaining interest as an approach to potentially overcome these modeling challenges within most computational electromagnetics algorithms [17–26]. There is a long history

of using different kinds of potential-based formulations that utilize various gauge conditions in FEM implementations for several purposes (e.g., analyzing waveguides, preconditioning, etc.), with many examples discussed in [27]. Modern uses of this phrase typically refer to methods targeted at overcoming the low-frequency breakdown inherent in field-based approaches, and often focus on using some form of Lorenz gauge condition in the process. To date, FEM implementations within this modern perspective on potential-based formulations have only considered simple lumped excitations and terminating boundary conditions [19, 24, 28]. In this work, we theoretically and numerically investigate how wave port boundary conditions can be used in a full 3D Lorenz gauge potential-based FEM analysis [19] to improve the practicality of these solvers. Our theoretical analysis proves that traditional field-based wave port boundary conditions can be used directly in 3D Lorenz gauge potential-based FEM solvers. To aid in numerically validating this, we introduce a potential-based FEM approach for analyzing inhomogeneous waveguides that is formulated in the same Lorenz gauge as the 3D potential-based FEM solver of interest to compare properties of the wave port eigenvalue problems between Lorenz gauge potential- and field-based methods. We also analyze a 3D geometry using a 3D Lorenz gauge potential-based FEM solver that utilizes a traditional field-based wave port boundary condition and show that the results match that of a conventional 3D field-based FEM analysis.

The remainder of this work is organized as follows. In Section 2, we analyze the spectral properties of the field- and Lorenz gauge potential-based eigenvalue problems to determine their theoretical properties. Through this analysis, we prove that any field-based FEM solution for an inhomogeneous waveguide problem can be used in a wave port boundary condition for a Lorenz gauge potential-based method. Then, in Section 3, we present the development of an FEM discretization of the Lorenz gauge potential-based eigenvalue problem that will be used to verify the theoretical claims made in Section 2. We also note in this section details on unique null spaces in the 2D formulation of waveguide problems that prevents the Lorenz gauge potential-based method from being useful for practical analysis of inhomogeneous waveguides. However, the method is still necessary to numerically validate the various theoretical claims made throughout this work, which is done in Section 4. Finally, we present conclusions in Section 5.

2. PROPERTIES OF THE EIGENVALUE PROBLEMS

In this section, relevant spectral properties of the eigenvalue problems considered in this work are theoretically analyzed. We begin in Section 2.1 by reviewing preliminary material related to the governing wave equations of interest and their corresponding boundary conditions. Following this, we specialize the analysis in Section 2.2 to consider waveguiding geometries to analyze the desired spectral properties.

2.1. Preliminaries

In a lossless, source-free inhomogeneous medium, Maxwell's equations can be combined into a wave equation to get

$$\nabla \times \frac{1}{\mu_r}\nabla \times \mathbf{E} - k_0^2\epsilon_r\mathbf{E} = 0, \tag{1}$$

where μ_r is the relative permeability, ϵ_r the relative permittivity, and $k_0^2 = \omega^2\mu_0\epsilon_0$. Alternatively, the magnetic vector potential $\mathbf{A}$ and electric scalar potential Φ can be introduced in the typical fashion so that $\mathbf{B} = \nabla \times \mathbf{A}$ and $\mathbf{E} = -j\omega\mathbf{A} - \nabla\Phi$. In terms of the potentials, Maxwell's equations become a set of two coupled partial differential equations. In many instances it is convenient to decouple the potentials into separate partial differential equations through an appropriate choice of gauge condition. Using the particular Lorenz gauge

$$\nabla \cdot \epsilon_r\mathbf{A} = -j\omega\mu_0\epsilon_0\Phi, \tag{2}$$

the governing wave equations for $\mathbf{A}$ and Φ can be easily found to be [17]

$$\nabla \times \frac{1}{\mu_r}\nabla \times \mathbf{A} - k_0^2\epsilon_r\mathbf{A} - \epsilon_r\nabla\nabla \cdot \epsilon_r\mathbf{A} = 0, \tag{3}$$

$$\nabla \cdot \epsilon_r\nabla\Phi + k_0^2\Phi = 0. \tag{4}$$

Note that (4) is not always needed because it is derivable from (3) in non-static cases, and because the solution for Φ can be recovered via the gauge condition (2) [26]. As will be elucidated later, this gauge condition also causes a component of $\mathbf{A}$ to exactly cancel with $\nabla\Phi$ in the computation of $\mathbf{E}$, making these contributions not of interest physically. Given this, and that (4) is a well-studied equation (e.g., [14]), we do not consider explicit solutions of (4) in this work.

Before moving on, it will be helpful to review the boundary conditions applicable to $\mathbf{A}$. Exhaustive accounts on standard boundary conditions for $\mathbf{A}$ can be found in various locations; e.g., [17, 26, 29, 30]. We will review only those of most relevance for this particular work. First, at material interfaces the tangential components of $\mathbf{A}$ should be continuous, which can be easily inferred from its relationship with $\mathbf{E}$. Similarly, at an interface with a perfect electric conductor (PEC) it can be determined that $\hat{n} \times \mathbf{A} = 0$. Additionally, one also has that on a PEC surface

$$\int_\Gamma \hat{n} \cdot \epsilon_r \mathbf{A} d\Gamma = 0, \tag{5}$$

where Γ denotes the surface of the PEC object [29]. This condition is synonymous with a charge neutrality constraint, which can be understood by considering how $\hat{n} \cdot \epsilon_r \mathbf{A}$ is related to the electric flux density. Finally, we must also consider the boundary condition appropriate for $\nabla \cdot \epsilon_r \mathbf{A}$. From the Lorenz gauge of (2), we see that the appropriate boundary condition will be that of Φ, which is that Φ equals a constant voltage [29]. Hence, we also have that $\nabla \cdot \epsilon_r \mathbf{A}$ is constant on a PEC surface.

2.2. Spectral Properties

When considering waveguide geometries that are invariant along the propagation direction (taken to be the z-direction in this work), the problem can be reduced to analyzing a 2D cross section of the waveguide by searching for solutions in the general form of

$$\mathbf{F} = [\mathbf{f}_t(x,y) + \hat{z} f_z(x,y)] e^{-j\beta z}, \tag{6}$$

where $\mathbf{F}$ can be either $\mathbf{E}$ or $\mathbf{A}$; $\mathbf{f}_t$ are the transverse components; f_z is the longitudinal component; and β is the phase constant [31]. Upon substituting (6) into either (1) or (3), an eigenvalue problem can be established to solve for the allowable β and mode profiles defined by $\mathbf{f}_t$ and f_z.

To establish theoretical results relevant to wave port boundary conditions, it will be useful to examine some of the spectral properties of (1) and (3) as eigenvalue problems in a generic closed 3D region. After establishing these general properties, we can conclude that they will also hold for the specific case of (6) for a particular β. Considering this, the generalized eigenvalue problems of interest are

$$\nabla \times \frac{1}{\mu_r} \nabla \times \mathbf{E}_m = \omega_m^2 \epsilon_r \mathbf{E}_m, \tag{7}$$

$$\nabla \times \frac{1}{\mu_r} \nabla \times \mathbf{A}_m - \epsilon_r \nabla \nabla \cdot \epsilon_r \mathbf{A}_m = \nu_m^2 \epsilon_r \mathbf{A}_m, \tag{8}$$

where ω_m^2 and ν_m^2 are the eigenvalues, and $\mathbf{E}_m$ and $\mathbf{A}_m$ are the corresponding eigenvectors.

To begin, we establish that there is no overlap between the null spaces of the two differential operators on the left-hand side of (8) for eigenvectors with non-zero eigenvalues. To aid in this, we define two additional eigenvalue problems as

$$\nabla \times \frac{1}{\mu_r} \nabla \times \mathbf{A}_{\perp,m} = \nu_{\perp,m}^2 \epsilon_r \mathbf{A}_{\perp,m}, \tag{9}$$

$$-\epsilon_r \nabla \nabla \cdot \epsilon_r \mathbf{A}_{\|,m} = \nu_{\|,m}^2 \epsilon_r \mathbf{A}_{\|,m}. \tag{10}$$

By taking the divergence of (9), we find that

$$0 = \nu_{\perp,m}^2 \nabla \cdot \epsilon_r \mathbf{A}_{\perp,m}. \tag{11}$$

So long as $\nu_{\perp,m}^2 \neq 0$, we see that all eigenvectors $\mathbf{A}_{\perp,m}$ of (9) are in the null space of the eigenvalue problem (10). Similarly, we can divide (10) by ϵ_r and take the curl to find that

$$0 = \nu_{\|,m}^2 \nabla \times \mathbf{A}_{\|,m}. \tag{12}$$

Again, so long as $\nu_{\parallel,m}^2 \neq 0$, we see that all eigenvectors $\mathbf{A}_{\parallel,m}$ of (10) are in the null space of the eigenvalue problem (9).

This result shows that any eigenvector $\mathbf{E}_m$ of (7) with eigenvalue $\omega_m^2 \neq 0$ will also be an eigenvector of (8) with the same eigenvalue ω_m^2. This establishes that all solutions of the field-based problem (7) will also be solutions to the potential-based problem (8). However, it is also necessary to show that this set of solutions is sufficient for exciting a potential-based analysis, which can be established by showing the two families of eigenvectors $\mathbf{A}_{\perp,m}$ and $\mathbf{A}_{\parallel,m}$ are bases for the null spaces of their complementary problems. If this is the case, we see that the only additional solutions to (8) produce zero electric and magnetic fields, and so are not of physical interest as excitations to a simulation.

To show that the two families of eigenvectors can serve as bases, we demonstrate that the differential operators on the left-hand sides of (9) and (10) are self-adjoint with respect to an L^2 inner product [32]. Given this, each operator then possesses a complete set of mutually orthogonal eigenvectors that can be used to expand any function within its domain of operation.

We begin with (9), with the inner product being

$$\langle \mathbf{u}, L_1 \mathbf{v} \rangle = \int_\Omega \mathbf{u}^* \cdot L_1 \mathbf{v} d\Omega, \tag{13}$$

where $L_1 = \nabla \times 1/\mu_r \nabla \times \cdot$ and Ω is the entire domain of the problem being considered. To show that L_1 is self-adjoint, we integrate by parts twice and use the divergence theorem to get

$$\langle \mathbf{u}, L_1 \mathbf{v} \rangle = \int_\Omega \mathbf{v} \cdot \nabla \times \frac{1}{\mu_r} \nabla \times \mathbf{u}^* d\Omega + \int_\Gamma \hat{n} \cdot \left(\frac{1}{\mu_r} (\nabla \times \mathbf{v}) \times \mathbf{u}^* + \mathbf{v} \times \frac{1}{\mu_r} (\nabla \times \mathbf{u}^*) \right) d\Gamma, \tag{14}$$

where Γ is the boundary surface of the closed region Ω.

Various choices for boundary conditions can be applied to $\mathbf{u}$ and $\mathbf{v}$ to ensure that L_1 is self-adjoint. For an inhomogeneous waveguide problem, it is typical to consider that the waveguide is "shielded" by placing a continuous PEC boundary around the outer wall of the waveguide. Adopting this choice here, we will have that $\hat{n} \times \mathbf{v} = 0$ and $\hat{n} \times \mathbf{u}^* = 0$ on Γ. With this boundary condition, the boundary integrals in (14) vanish and we are left with

$$\langle \mathbf{u}, L_1 \mathbf{v} \rangle = \int_\Omega \mathbf{v} \cdot \nabla \times \frac{1}{\mu_r} \nabla \times \mathbf{u}^* d\Omega = \langle L_1 \mathbf{u}, \mathbf{v} \rangle, \tag{15}$$

which establishes the self-adjoint property of L_1.

A similar process can now be used to show that $L_2 = -\epsilon_r \nabla \nabla \cdot \epsilon_r \cdot$ is self-adjoint. We begin by integrating by parts twice and using the divergence theorem to get

$$\langle \mathbf{u}, L_2 \mathbf{v} \rangle = \langle L_2 \mathbf{u}, \mathbf{v} \rangle - \int_\Omega \hat{n} \cdot (\epsilon_r \mathbf{u}^* \nabla \cdot \epsilon_r \mathbf{v} - \epsilon_r \mathbf{v} \nabla \cdot \epsilon_r \mathbf{u}^*) \, d\Omega. \tag{16}$$

Specifying physically meaningful boundary conditions that make the boundary terms vanish is more involved here than for (14). From the discussion in Section 2.1, we know that $\nabla \cdot \epsilon_r \mathbf{v}$ and $\nabla \cdot \epsilon_r \mathbf{u}^*$ will be constants on the PEC surfaces. If there is only one PEC, we can choose this as our reference (i.e., "ground") so that the constant voltage would be zero and naturally cause the boundary terms in (16) to vanish. If there are additional PECs not connected to the reference conductor, we can then factor the constant terms outside of the integrals so that our boundary terms become

$$-\nabla \cdot \epsilon_r \mathbf{v} \int_\Gamma \hat{n} \cdot \epsilon_r \mathbf{u}^* d\Gamma + \nabla \cdot \epsilon_r \mathbf{u}^* \int_\Gamma \hat{n} \cdot \epsilon_r \mathbf{v} d\Gamma. \tag{17}$$

From the charge neutrality constraint discussed in (5), we see that all boundary terms in (16) will vanish. As a result, we have that

$$\langle \mathbf{u}, L_2 \mathbf{v} \rangle = -\int_\Omega \mathbf{v} \cdot \epsilon_r \nabla \nabla \cdot \epsilon_r \mathbf{u}^* d\Omega = \langle L_2 \mathbf{u}, \mathbf{v} \rangle, \tag{18}$$

proving the self-adjoint property of the L_2 operator.

Having shown that both L_1 and L_2 are self-adjoint operators, we have established the desired property that each operator's set of eigenvectors is complete in their respective Hilbert spaces of

interest [32]. Combining this with the fact that the null spaces of L_1 and L_2 do not overlap, we also see that any null vector of either L_1 or L_2 with non-zero eigenvalue will not be in the null space of $L_1 + L_2$. As a result, the operator $L_1 + L_2$ is relatively well-conditioned, which is in sharp contrast to the significant ill-conditioning of the L_1 operator. This ill-conditioning is the origin of the low-frequency breakdown of traditional field-based FEM solvers. Hence, potential-based FEM solvers that successfully discretize $L_1 + L_2$ are free from the low frequency breakdown, as shown for a set of geometries in [19].

With respect to the physical meanings of the $\mathbf{A}_\perp$ and $\mathbf{A}_\parallel$ components of $\mathbf{A}$, it is useful to consider how they contribute to the computation of $\mathbf{B}$ and $\mathbf{E}$. As will be shown, only the $\mathbf{A}_\perp$ component contributes to physically measurable fields in the Lorenz gauge. To see this, we first trivially note that from (12) we have that $\mathbf{A}_\parallel$ will produce no $\mathbf{B}$, and so we recognize $\mathbf{B}$ is completely due to the $\mathbf{A}_\perp$ component. For $\mathbf{E}$, it is helpful to first recognize that due to (11) the Lorenz gauge condition only ties the $\mathbf{A}_\parallel$ component to Φ. This allows us to write the computation of $\mathbf{E}$ in terms of the potentials as

$$\mathbf{E} = -j\omega\mathbf{A} - \nabla\Phi = -j\omega(\mathbf{A}_\perp + \mathbf{A}_\parallel) + \frac{1}{j\omega\mu_0\epsilon_0}\nabla\nabla\cdot\epsilon_r\mathbf{A}_\parallel. \tag{19}$$

From (3), we conclude that $\nabla\nabla\cdot\epsilon_r\mathbf{A}_\parallel = -k_0^2\mathbf{A}_\parallel$. Using this result in (19), we immediately see that $\mathbf{E} = -j\omega\mathbf{A}_\perp$, showing that all measurable fields are only due to $\mathbf{A}_\perp$. This provides another interpretation for why in many situations it is not necessary to explicitly compute Φ by solving (4).

3. POTENTIAL-BASED FEM FORMULATION

We will now consider the development of potential-based FEM solvers for analyzing inhomogeneous waveguides to aid in validating the theoretical claims made in the previous section. We begin in Section 3.1 by considering simply-connected geometries that admit a relatively standard discretization approach. Following this, we will have the proper context to discuss the issues with multiply-connected geometries in Section 3.2 that make this method not practical for general use cases. Despite these issues for practical situations, the method of Section 3.1 is still needed to verify the theoretical claims made in Section 2.

3.1. Simply-Connected Case

To begin, we note that the weak form for the vector wave equation given in (3) can be easily found to be

$$\int_\Omega \left[\frac{1}{\mu_r}\left(\nabla\times\mathbf{W}^*\right)\cdot\left(\nabla\times\mathbf{A}\right) - k_0^2\epsilon_r\mathbf{W}^*\cdot\mathbf{A} - \epsilon_r\mathbf{W}^*\cdot\nabla\nabla\cdot\epsilon_r\mathbf{A}\right] d\Omega = 0, \tag{20}$$

where $\mathbf{W}$ is the testing function. The FEM discretization of the final term requires more care because the divergence of a typical edge element basis function is zero. To handle this issue, we follow the example of [19] and temporarily introduce an auxiliary unknown $P = \nabla\cdot\epsilon_r\mathbf{A}$ that is proportional to the scalar potential. The weak form wave equation then becomes

$$\int_\Omega \left[\frac{1}{\mu_r}\left(\nabla\times\mathbf{W}^*\right)\cdot\left(\nabla\times\mathbf{A}\right) - k_0^2\epsilon_r\mathbf{W}^*\cdot\mathbf{A} - \epsilon_r\mathbf{W}^*\cdot\nabla P\right] d\Omega = 0. \tag{21}$$

We then expand our various functions along similar lines to the traditional field-based approach as [1, 14]

$$\mathbf{A} = \left[\frac{1}{\beta}\mathbf{a}_t(x,y) + j\hat{z}a_z(x,y)\right]e^{-j\beta z}, \tag{22}$$

$$P = \frac{1}{\beta}p(x,y)e^{-j\beta z}, \tag{23}$$

$$\mathbf{W}^* = \left[\frac{1}{\beta}\mathbf{w}_t(x,y) - j\hat{z}w_z(x,y)\right]e^{j\beta z}. \tag{24}$$

Substituting these expressions into (21) and simplifying yields

$$\int_\Omega \left\{ \frac{1}{\beta^2} \frac{1}{\mu_r} (\nabla_t \times \mathbf{w}_t) \cdot (\nabla_t \times \mathbf{a}_t) - \frac{1}{\beta^2} k_0^2 \epsilon_r \mathbf{w}_t \cdot \mathbf{a}_t + \frac{1}{\mu_r} (\mathbf{w}_t + \nabla_t w_z) \cdot (\mathbf{a}_t + \nabla_t a_z) \right.$$
$$\left. - k_0^2 \epsilon_r w_z a_z - \frac{1}{\beta^2} \epsilon_r \mathbf{w}_t \cdot \nabla_t p + \epsilon_r w_z p \right\} d\Omega = 0, \tag{25}$$

where ∇_t is a transverse differential operator [31].

We now look at how to eliminate the auxiliary variable P. To do this, we solve for P in terms of $\mathbf{A}$ in a weak sense [19]. In particular, we test $P = \nabla \cdot \epsilon_r \mathbf{A}$ with a testing function

$$Q^* = \frac{1}{\beta} q(x, y) e^{j\beta z} \tag{26}$$

to get

$$\int_\Omega \frac{1}{\beta} q e^{j\beta z} \nabla \cdot \epsilon_r \mathbf{A} \, d\Omega = \int_\Omega = \frac{1}{\beta^2} qp \, d\Omega. \tag{27}$$

Next, we integrate by parts and substitute in the explicit expression for $\mathbf{A}$ from (22) to get

$$-\int_\Omega \epsilon_r \left(\frac{1}{\beta} \nabla_t q + j\hat{z} q \right) \cdot \left(\frac{1}{\beta} \mathbf{a}_t + j\hat{z} a_z \right) d\Omega = \int_\Omega \frac{1}{\beta^2} qp \, d\Omega, \tag{28}$$

which can be simplified to

$$\int_\Omega \left[-\frac{1}{\beta^2} \epsilon_r \nabla_t q \cdot \mathbf{a}_t + \epsilon_r q a_z \right] d\Omega = \int_\Omega \frac{1}{\beta^2} qp \, d\Omega. \tag{29}$$

We can solve (29) with FEM by expanding

$$\mathbf{a}_t(x, y) = \sum_{n=1}^{N_{\text{edge}}} a_{t,n} \mathbf{N}_n(x, y), \tag{30}$$

$$a_z(x, y) = \sum_{n=1}^{N_{\text{node}}} a_{z,n} N_n(x, y), \tag{31}$$

where $\mathbf{N}_n$ is the nth edge element, and N_n is the nth linear nodal function typically used in scalar FEM [14]. Similarly, p can be expanded as in (31). Using a Galerkin testing approach, the matrix form of (29) becomes

$$\begin{bmatrix} -K_{zt,\epsilon} & \beta^2 G_{zz,\epsilon} \end{bmatrix} \begin{Bmatrix} a_t \\ a_z \end{Bmatrix} = [G_{zz}] \{p\}, \tag{32}$$

where the matrix elements are given by

$$K_{zt,\epsilon;mn} = \int_\Omega \epsilon_r \nabla_t N_m \cdot \mathbf{N}_n d\Omega, \tag{33}$$

$$G_{zz;mn} = \int_\Omega N_m N_n d\Omega, \tag{34}$$

$$G_{zz,\epsilon;mn} = \int_\Omega \epsilon_r N_m N_n d\Omega. \tag{35}$$

We can then solve (32) to find

$$\{p\} = \begin{bmatrix} -G_{zz}^{-1} K_{zt,\epsilon} & \beta^2 G_{zz}^{-1} G_{zz,\epsilon} \end{bmatrix} \begin{Bmatrix} a_t \\ a_z \end{Bmatrix}. \tag{36}$$

Returning to the full formulation of (25), we can find that the matrix form of the terms involving p is

$$\begin{bmatrix} -(1/\beta^2) K_{tz,\epsilon} \\ G_{zz,\epsilon} \end{bmatrix} \{p\}, \tag{37}$$

where

$$K_{tz,\epsilon;mn} = \int_\Omega \epsilon_r \mathbf{N}_m \cdot \nabla_t N_n d\Omega. \tag{38}$$

The auxiliary unknown $\{p\}$ can now be completely eliminated by using (36) to get

$$\begin{bmatrix} -(1/\beta^2)K_{tz,\epsilon} \\ G_{zz,\epsilon} \end{bmatrix} \begin{bmatrix} -G_{zz}^{-1}K_{zt,\epsilon} & \beta^2 G_{zz}^{-1}G_{zz,\epsilon} \end{bmatrix} \begin{Bmatrix} a_t \\ a_z \end{Bmatrix}$$

$$= \begin{bmatrix} -(1/\beta^2)K_{tz,\epsilon}G_{zz}^{-1}K_{zt,\epsilon} & -K_{tz,\epsilon}G_{zz}^{-1}G_{zz,\epsilon} \\ -G_{zz,\epsilon}G_{zz}^{-1}K_{zt,\epsilon} & \beta^2 G_{zz,\epsilon}G_{zz}^{-1}G_{zz,\epsilon} \end{bmatrix} \begin{Bmatrix} a_t \\ a_z \end{Bmatrix}. \tag{39}$$

This can be combined with the remaining matrix form of (25) to arrive at the final generalized eigenvalue problem of

$$\begin{bmatrix} K_{2,\mu} & K_{tz,\mu} - K_{tz,\epsilon}G_{zz}^{-1}G_{zz,\epsilon} \\ 0 & G_{zz,\epsilon}G_{zz}^{-1}G_{zz,\epsilon} \end{bmatrix} \begin{Bmatrix} a_t \\ a_z \end{Bmatrix} = -\frac{1}{\beta^2} \begin{bmatrix} K_1 - k_0^2 K_{2,\epsilon} + K_{tz,\epsilon}G_{zz}^{-1}K_{zt,\epsilon} & 0 \\ K_{zt,\mu} - G_{zz,\epsilon}G_{zz}^{-1}K_{zt,\epsilon} & S_1 - k_0^2 G_{zz,\epsilon} \end{bmatrix} \begin{Bmatrix} a_t \\ a_z \end{Bmatrix}, \tag{40}$$

where

$$K_{1;mn} = \int_\Omega \frac{1}{\mu_r} (\nabla_t \times \mathbf{N}_m) \cdot (\nabla_t \times \mathbf{N}_n) d\Omega, \tag{41}$$

$$K_{2,\mu;mn} = \int_\Omega \frac{1}{\mu_r} \mathbf{N}_m \cdot \mathbf{N}_n d\Omega, \tag{42}$$

$$K_{2,\epsilon;mn} = \int_\Omega \epsilon_r \mathbf{N}_m \cdot \mathbf{N}_n d\Omega, \tag{43}$$

$$K_{tz,\mu;mn} = \int_\Omega \frac{1}{\mu_r} \mathbf{N}_m \cdot \nabla_t N_n d\Omega, \tag{44}$$

$$K_{zt,\mu;mn} = \int_\Omega \frac{1}{\mu_r} \nabla_t N_m \cdot \mathbf{N}_n d\Omega, \tag{45}$$

$$S_{1;mn} = \int_\Omega \frac{1}{\mu_r} \nabla_t N_m \cdot \nabla_t N_n d\Omega. \tag{46}$$

As will be shown in Section 4, it is interesting to note that the generalized eigenvalue problem of (40) does not support trivial $\beta^2 = 0$ modes, which are not physical but are present in traditional formulations [1, 3, 8]. These trivial modes slow convergence in standard iterative solvers, requiring the development of specialized eigensolvers to avoid this issue. Eliminating these trivial modes directly through the equations employed allows for a wider range of advanced iterative solvers to be used in the solution of (40) without any further special treatment.

3.2. Multiply-Connected Case

We will now consider the case of a multiply-connected geometry for the potential-based FEM formulation. A simple example of this kind of structure would be a microstrip trace made of PEC. In this case, the signal conductor puts a single "hole" in the 2D geometry that changes the topology of the region. This "hole" causes issues for the potential-based FEM formulation introduced in Section 3.1 by adding an element into the null space of the discretized L_1 operator that is not able to be removed by the discretized L_2 operator. As mentioned previously, this causes this method to not be useful for many practical use cases. However, it is still needed to provide sufficient numerical validation for the theoretical claims made throughout this work. It should also be emphasized that this issue is unique to the 2D case, and does not affect general-purpose 3D Lorenz gauge potential-based methods [19, 26].

The origin of the issue for multiply-connected geometries is the boundary condition that must be enforced on the additional PEC region. Recalling the discussion in Section 2, $\nabla \cdot \epsilon_r \mathbf{A}$ must equal a constant on all PEC surfaces of the geometry. When there is only a single PEC region this causes no issue because the voltage of this PEC can be set to zero. However, when more distinct PEC regions are in the geometry (making the 2D cross-section multiply-connected) $\nabla \cdot \epsilon_r \mathbf{A}$ needs to equal some non-zero

constant along each non-reference conductor. As a result, the auxiliary unknown $P = \nabla \cdot \epsilon_r \mathbf{A}$ cannot be expanded like in (23).

Naively setting the voltage on all PEC regions to zero so that P can be expanded with (23) leads to a generalized eigenvalue problem that has a null space with dimension equaling the number of "holes" in the 2D geometry. The resulting method exhibits a low-frequency breakdown, but is otherwise accurate at middle frequencies, as will be shown in Section 4. Attempting to allow the PEC objects to support a non-zero voltage while still using (23) to expand P leads to a method with no null space, but which produces inaccurate physical results at all frequencies (this is not shown for brevity).

4. NUMERICAL RESULTS

In this section, we present the results from a number of numerical examples to verify different claims made throughout this work. We begin in Section 4.1 by presenting results for simply-connected geometries. Following this, we demonstrate the issues with multiply-connected geometries in Section 4.2. Finally, we discuss the results of using a field-based wave port as a boundary condition for a 3D Lorenz gauge potential-based FEM solver in Section 4.3.

For all numerical results that are compared to an analytical solution, we utilize an iterative eigenvalue problem solver to only compute a small number of eigenvalues and eigenvectors to mimic a more practical use case. The particular iterative method we use is the Krylov-Schur algorithm described in [33], which is implemented in Matlab as the eigs function. When we compute all the eigenvalues or singular values of the system, we utilize other standard algorithms designed for computing the full decompositions.

4.1. Simply-Connected Case

To begin, we consider two simple geometries that have analytical solutions to validate the accuracy of the potential-based FEM formulation presented in Section 3.1. The first is an empty circular waveguide and the second is a rectangular waveguide half-filled with a dielectric material with $\epsilon_r = 4$. In each case, we normalize various quantities with respect to dimensions of the waveguide to plot universal dispersion curves for the first few propagating modes, which are shown in Fig. 1. As expected, very good agreement is achieved between the potential-based FEM and analytical results.
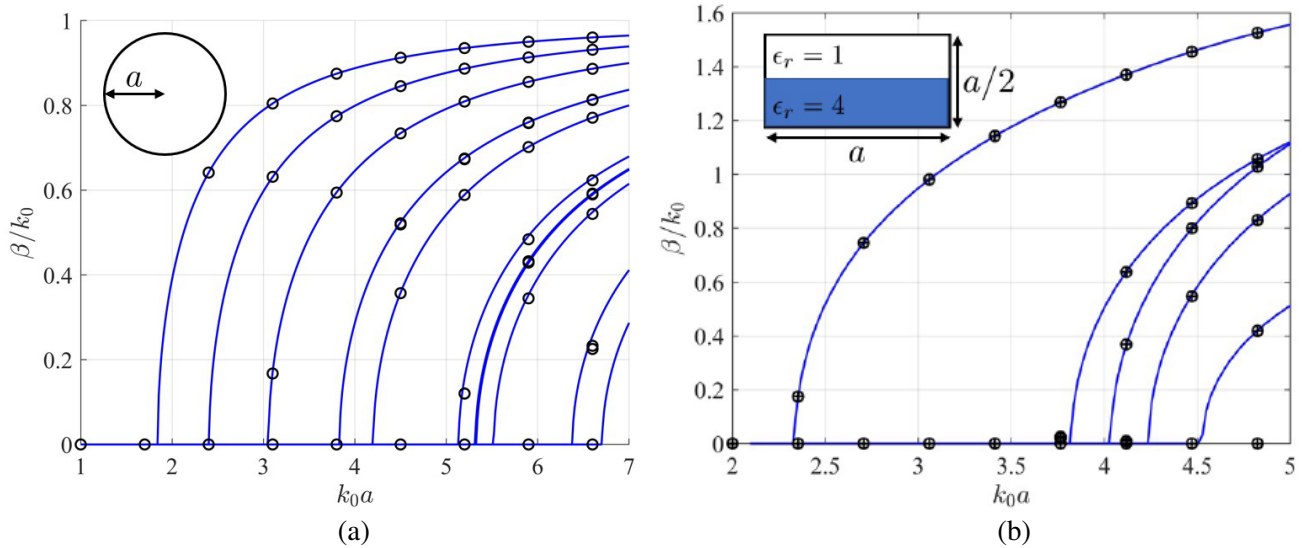

Figure 1. Normalized propagation constant for (a) an empty circular waveguide and (b) a half-filled rectangular waveguide, with geometric details shown in the insets. Solid lines are the analytical solution and circles are from the potential-based FEM formulation. In (b), pluses are from the potential-based FEM that uses a SAI (see main text for details).

For large scale computations, it is impractical to calculate G_{zz}^{-1} as it ruins the sparsity of the matrix system and is computationally inefficient. To alleviate this, it has been found that the accuracy and other advantageous properties of potential-based FEM formulations can be maintained if a sparse approximate inverse (SAI) is used instead of G_{zz}^{-1} [19]. We test this here on the half-filled rectangular waveguide geometry by using the SAI algorithm from [34] that is parallelizable and adaptively finds a sparsity pattern for the SAI.

As initial settings, we allow the SAI to have a fill-in of 30 elements per row (G_{zz} is a 1001×1001 matrix for this geometry), where the fill-in number sets a "soft" maximum on the number of non-zero elements in each row. For this case, the SAI achieved a 98.28% sparsity. We found that with these settings a negligible change in accuracy occurred, as shown in Fig. 1(b). We also ran further tests for different fill-in numbers, and found that a comparable accuracy was achieved until the fill-in was dropped from 15 to 10 (from 99.12% to 99.41% sparsity). This highlights that this technique can also be used in solving eigenvalue problems, but more extensive testing on a wider range of geometries is warranted to determine what settings are sufficiently robust for practical use.

Next, we demonstrate that the potential-based FEM formulation does not support trivial $\beta^2 = 0$ modes. To show this, we plot in Fig. 2 the relative magnitude of β^2 for all eigenvectors of the potential-based formulation of (40), the version using the SAI with a fill-in of 30 elements per row, and for a traditional field-based formulation described in [1, 14]. It is clear that the field-based formulation supports a large number of trivial modes, which are due to the null space of the L_1 operator. It is known that the number of such null modes matches the number of internal nodes of the computational domain [11], which is found to be the case for this geometry. In contrast to this, the potential-based formulation supports no such modes due to the spectral properties of the $L_1 + L_2$ operator that were discussed in Section 2. We also see that the results using a SAI are effectively identical to those using the full G_{zz}^{-1}, indicating that the SAI does not significantly affect the spectral properties of the potential-based formulation.
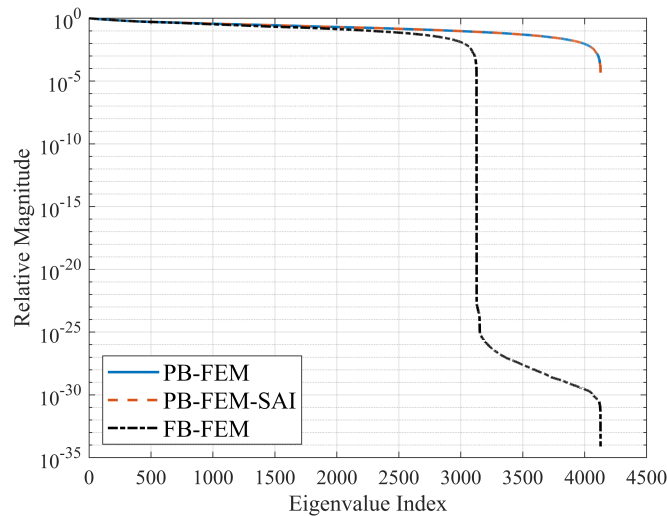

Figure 2. Comparison of the relative magnitude of β^2 for the half-filled rectangular waveguide when using the potential-based FEM (PB-FEM), the potential-based FEM using a SAI (PB-FEM-SAI), and traditional field-based FEM (FB-FEM) formulations.

As a final example, we show that the eigenvectors of the potential-based FEM formulation closely match those of the traditional field-based approach of [1] for a more complicated inhomogeneous waveguide that does not support an analytical solution (geometry shown as an inset in Fig. 3(b)). As discussed in Section 2, this comparison is only applicable for the subset of eigenvectors of the potential-based FEM formulation that are eigenvectors of the L_1 operator. To check the similarity of the eigenvectors, we first identify the potential- and field-based eigenvectors that have approximately the same eigenvalue and that are most similar to one another. We then perform any constant re-scaling
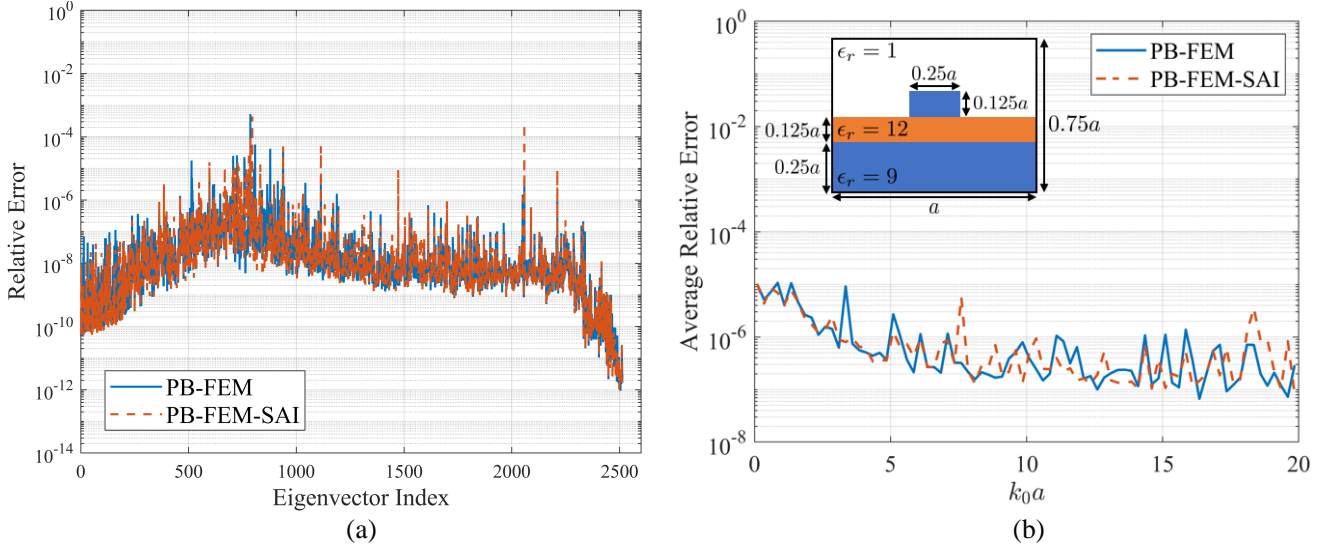
Figure 3. Relative error between the potential-based and field-based eigenvectors of the L_1 operator. (a) Relative error for each eigenvector at $k_0a = 10.1$ and (b) average relative error for all eigenvectors as a function of k_0a. The geometry analyzed is shown as an inset in (b).

that is needed (e.g., due to a complex phase) so that the relative error can be computed. We compute the relative ℓ^2-error between the two eigenvectors as

$$\text{Relative Error} = \frac{||\mathbf{v}_{\text{FB}} - \mathbf{v}_{\text{PB}}||_2}{||\mathbf{v}_{\text{FB}}||_2}, \tag{47}$$

where $\mathbf{v}_{\text{FB}}$ and $\mathbf{v}_{\text{PB}}$ are the field-based and potential-based eigenvectors, respectively.

We show this relative error for each of the relevant eigenvectors in Fig. 3(a) for a simulation at $k_0a = 10.1$, where the eigenvectors have been sorted in a descending fashion according to the magnitude of their eigenvalue. We see that overall, the relative error is generally small between the potential- and field-based FEM formulations. The increase in relative error toward the middle of the curves is primarily due to mixing of degenerate $\mathbf{A}_{\perp,m}$ and $\mathbf{A}_{\parallel,m}$ modes in the potential-based method. These modes can be separated numerically if need, but this is not necessary for the current purposes so is not performed. We also perform this comparison for the potential-based formulation using a SAI with a fill-in of 30 elements per row (G_{zz} is a 804×804 matrix) and find similar results.

To monitor these results as a function of k_0a, we compute the average relative error for all of the relevant eigenvectors at a given value of k_0a. These results are shown in Fig. 3(b) for $0.1 \leq k_0a \leq 19.85$, where it is seen that the average relative error is largely consistent. There is an increase in error as k_0a becomes smaller, which is believed to occur because most of the modes in the waveguide are below cutoff and the corresponding number of degenerate $\mathbf{A}_{\perp,m}$ and $\mathbf{A}_{\parallel,m}$ modes increases.

4.2. Multiply-Connected Case

We now present numerical results illustrating the issues with the formulation of Section 3 for multiply-connected geometries. First, we show how the size of the numerical null space grows with the number of "holes" in the geometry for a naive potential-based FEM formulation that enforces $P = \nabla \cdot \epsilon_r \mathbf{A} = 0$ on all PEC surfaces. In particular, we inspect the singular value spectra of the matrix on the right-hand side of (40) for a microstrip geometry with one to three signal traces, where each signal trace produces a new "hole" in the geometry. A schematic of the simulated geometry with a single signal trace is shown in Fig. 4. These parameters are also representative for the other microstrip geometries, with the two (three) signal trace case having an inter-trace distance of $40\,\mu\text{m}$ ($20\,\mu\text{m}$). The corresponding singular value spectra are shown in Fig. 5, where it is clearly seen that one extremely small singular value exists for each "hole" in the geometry being considered.
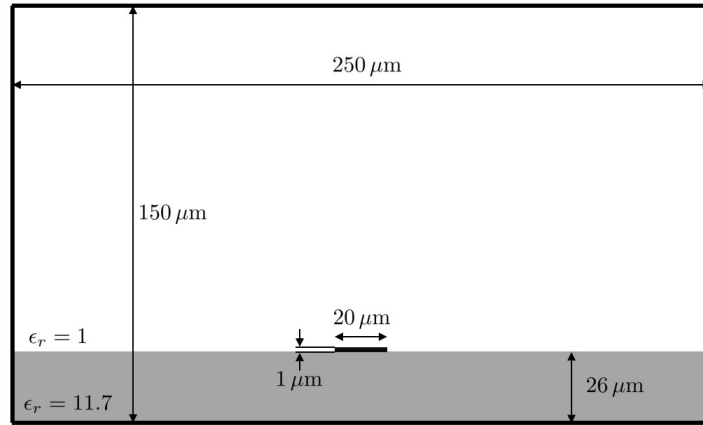
Figure 4. Schematic of the single microstrip trace geometry. Thick black lines denote a PEC boundary condition.
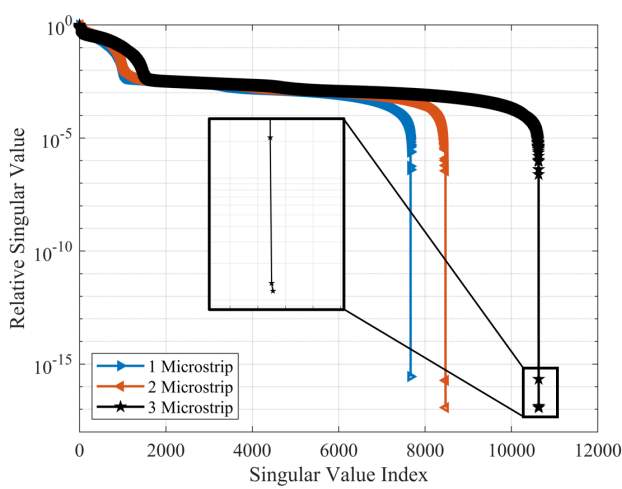

Figure 5. Comparison of the singular value spectrum of the potential-based FEM formulation for geometries with different numbers of "holes". Markers are placed at each actual data point making up a line to highlight the number of very small singular values matches the number of "holes" in the geometry.
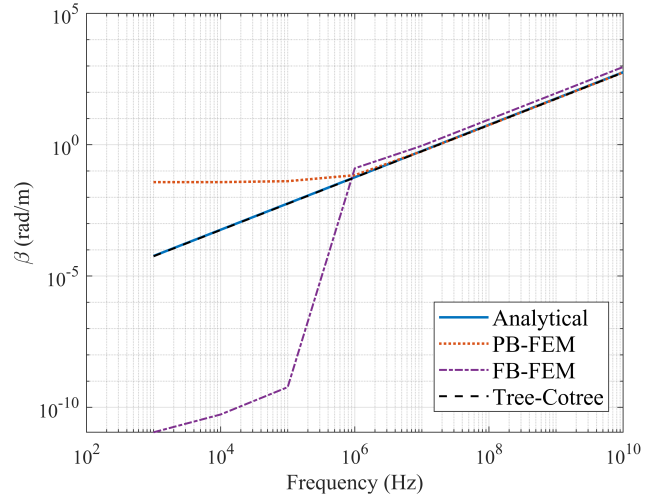
Figure 6. Comparison of the phase constant of a microstrip geometry as a function of frequency using various FEM formulations. Only the tree-cotree method maintains accuracy over the entire set of frequencies simulated.

Next, we simulate the microstrip geometry with a single trace over a broad range of frequencies to demonstrate that the presence of any extremely small singular values leads to a low-frequency breakdown. We compare the solution to an analytical prediction based on quasistatic approximations [35], a traditional field-based formulation [1], and a low-frequency stabilized traditional formulation [8]. In particular, the low-frequency stabilized formulation utilizes a tree-cotree splitting within a potential-based formulation that utilizes a different gauge from the standard Lorenz gauge [8]. From the results in Fig. 6, it is clear that only the formulation from [8] maintains accuracy over the entire frequency sweep. We also note that the frequency where a catastrophic breakdown occurs in the numerical results is consistent with the analytical estimation [16]

$$\frac{(\omega\ell)^2}{10^{17}} > 10^{-16},\tag{48}$$

where ℓ is the average edge length of the mesh.

These examples clearly demonstrate the issues with using a straightforward discretization like that discussed in Section 3.1 for multiply-connected geometries. As a result, this potential-based FEM formulation is not suitable for use in many practical scenarios. This is unfortunate, since having a method that does not support trivial $\beta^2 = 0$ eigenvalues would be beneficial for improving the convergence of iterative methods without the need of specialized eigensolvers [1, 3, 8]. However, because any traditional formulation can be used as part of a wave port boundary condition for a 3D Lorenz gauge potential-based FEM formulation, this is not an issue for the continued development of these methods.

4.3. Wave Port Boundary Condition

As a final numerical example, we consider the use of a traditional formulation of a wave port boundary condition in a 3D Lorenz gauge potential-based FEM analysis to show that this can be successfully utilized. In particular, we analyze a rectangular waveguide geometry that has transverse dimensions of 22.86 mm × 10.16 mm and a longitudinal dimension of 40 mm. In the middle of the waveguide, there is a dielectric brick with transverse dimensions of 8 mm × 7 mm and a longitudinal dimension of 5 mm. The relative permittivity of the dielectric brick is selected as $\epsilon_r = 15$ to ensure there is a resonance in the scattering parameters of this geometry for the 9.5–10.5 GHz frequency band considered.

We use two wave port boundary conditions on either end of the rectangular waveguide based on the usual approach of [14, 15]. Although the mode distribution used is simply that of a TE_{10} mode, we still find this distribution numerically using the 2D FEM analysis of an inhomogeneous waveguide as detailed in [1] to emulate what would be done in practice. Using these wave ports, we calculate the scattering parameters when the 3D portion of the geometry is solved with the Lorenz gauge potential-based FEM discussed in [19]. These results are shown in Fig. 7, where they are also compared to the solution of the same problem using a traditional 3D field-based FEM analysis. As can be seen in Fig. 7, the agreement between the two methods is excellent. This shows that one can successfully use traditional wave port boundary conditions with a 3D Lorenz gauge potential-based FEM solver.
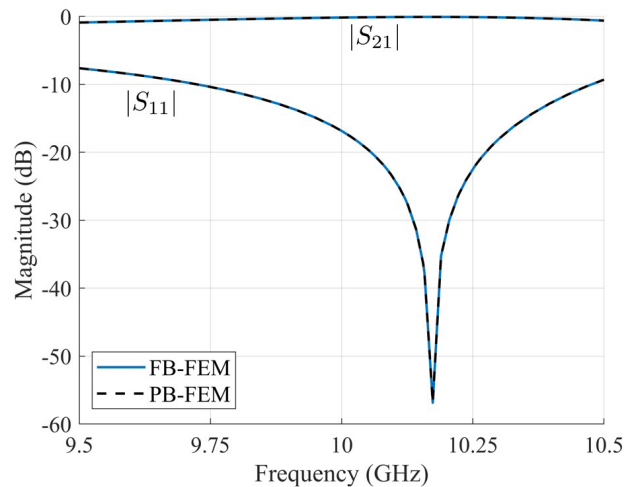

Figure 7. Comparison of the $|S_{11}|$ and $|S_{21}|$ of a rectangular waveguide geometry with a dielectric brick at its center. The waveguide is excited with a TE_{10} mode distribution using 3D Lorenz gauge potential-based and field-based solvers. Both 3D problems are excited using the same field-based wave port boundary condition.

5. CONCLUSIONS

In this work, we presented a theoretical and numerical analysis of how wave port boundary conditions can be utilized in 3D Lorenz gauge potential-based FEM solvers. By analyzing the properties of the relevant eigenvalue problems, we presented theoretical evidence that any traditional formulation for finding the modes of an inhomogeneous waveguide could be used in a wave port boundary condition for a 3D Lorenz gauge potential-based FEM formulation. To aid in numerically validating these theoretical claims, we also introduced a new 2D potential-based FEM formulation in the same Lorenz gauge as typical 3D solvers. Based on the numerical results demonstrated here, the widely useful wave port boundary condition can now be easily incorporated into 3D Lorenz gauge potential-based FEM formulations. These emerging methods have superior conditioning properties than traditional methods and do not require specialized treatments as the solver transitions between low- and high-frequency regimes. Hence, it can form the basis of a more robust 3D FEM solver than existing approaches in the future.

REFERENCES

1. Lee, J.-F., D.-K. Sun, and Z. J. Cendes, "Full-wave analysis of dielectric waveguides using tangential vector finite elements," *IEEE Transactions on Microwave Theory and Techniques*, Vol. 39, No. 8, 1262–1271, 1991.

2. Lee, J.-F., "Finite element analysis of lossy dielectric waveguides," *IEEE Transactions on Microwave Theory and Techniques*, Vol. 42, No. 6, 1025–1031, 1994.

3. Polstyanko, S. V., R. Dyczij-Edlinger, and J.-F. Lee, "Fast frequency sweep technique for the efficient analysis of dielectric waveguides," *IEEE Transactions on Microwave Theory and Techniques*, Vol. 45, No. 7, 1118–1126, 1997.

4. Selleri, S., L. Vincetti, A. Cucinotta, and M. Zoboli, "Complex FEM modal solver of optical waveguides with PML boundary conditions," *Optical and Quantum Electronics*, Vol. 33, No. 4, 359–371, 2001.

5. Savi, P., I.-L. Gheorma, and R. D. Graglia, "Full-wave high-order FEM model for lossy anisotropic waveguides," *IEEE Transactions on Microwave Theory and Techniques*, Vol. 50, No. 2, 495–500, 2002.

6. Vardapetyan, L. and L. Demkowicz, "Hp-vector finite element method for the full-wave analysis of waveguides with no spurious modes," *Electromagnetics*, Vol. 22, No. 5, 419–428, 2002.

7. Vardapetyan, L., L. Demkowicz, and D. Neikirk, "hp-vector finite element method for eigenmode analysis of waveguides," *Computer Methods in Applied Mechanics and Engineering*, Vol. 192, Nos. 1–2, 185–201, 2003.

8. Lee, S.-C., J.-F. Lee, and R. Lee, "Hierarchical vector finite elements for analyzing waveguiding structures," *IEEE Transactions on Microwave Theory and Techniques*, Vol. 51, No. 8, 1897–1905, 2003.

9. Lee, S.-H. and J.-M. Jin, "Application of the tree-cotree splitting for improving matrix conditioning in the full-wave finite-element analysis of high-speed circuits," *Microwave and Optical Technology Letters*, Vol. 50, No. 6, 1476–1481, 2008.

10. Beeckman, J., R. James, F. A. Fernández, W. De Cort, P. J. M. Vanbrabant, and K. Neyts, "Calculation of fully anisotropic liquid crystal waveguide modes," *Journal of Lightwave Technology*, Vol. 27, No. 17, 3812–3819, 2009.

11. Liu, N., G. Cai, C. Zhu, Y. Tang, and Q. H. Liu, "The mixed spectral-element method for anisotropic, lossy, and open waveguides," *IEEE Transactions on Microwave Theory and Techniques*, Vol. 63, No. 10, 3094–3102, 2015.

12. Liu, J., W. Jiang, N. Liu, and Q. H. Liu, "Mixed spectral-element method for the waveguide problem with Bloch periodic boundary conditions," *IEEE Transactions on Electromagnetic Compatibility*, Vol. 61, No. 5, 1568–1577, 2018.

13. Lin, X., G. Cai, H. Chen, N. Liu, and Q. H. Liu, "Modal analysis of 2-D material-based plasmonic waveguides by mixed spectral element method with equivalent boundary condition," *Journal of Lightwave Technology*, Vol. 38, No. 14, 3677–3686, 2020.

14. Jin, J.-M., *The Finite Element Method in Electromagnetics*, 3rd Edition, John Wiley & Sons, 2015.

15. Lee, S.-H. and J.-M. Jin, "Adaptive solution space projection for fast and robust wideband finite-element simulation of microwave components," *IEEE Microwave and Wireless Components Letters*, Vol. 17, No. 7, 474–476, 2007.

16. Zhu, J. and D. Jiao, "A theoretically rigorous full-wave finite-element-based solution of Maxwell's equations from DC to high frequencies," *IEEE Transactions on Advanced Packaging*, Vol. 33, No. 4, 1043–1050, 2010.

17. Chew, W. C., "Vector potential electromagnetics with generalized gauge for inhomogeneous media: Formulation," *Progress In Electromagnetics Research*, Vol. 149, 69–84, 2014.

18. Ryu, C. J., A. Y. Liu, W. E. I. Sha, and W. C. Chew, "Finite-difference time-domain simulation of the Maxwell-Schrödinger system," *IEEE Journal on Multiscale and Multiphysics Computational Techniques*, Vol. 1, 40–47, 2016.

19. Li, Y.-L., S. Sun, Q. I. Dai, and W. C. Chew, "Finite element implementation of the generalized-Lorenz gauged A-Φ formulation for low-frequency circuit modeling," *IEEE Transactions on Antennas and Propagation*, Vol. 64, No. 10, 4355–4364, 2016.

20. Vico, F., M. Ferrando, L. Greengard, and Z. Gimbutas, "The decoupled potential integral equation for time-harmonic electromagnetic scattering," *Communications on Pure and Applied Mathematics*, Vol. 69, No. 4, 771–812, 2016.

21. Liu, Q. S., S. Sun, and W. C. Chew, "A potential based integral equation method for low-frequency electromagnetic problems," *IEEE Transactions on Antennas and Propagation*, Vol. 66, No. 3, 1413–1426, 2018.

22. Roth, T. E. and W. C. Chew, "Development of stable A-Φ time domain integral equations for multiscale electromagnetics," *IEEE Journal on Multiscale and Multiphysics Computational Techniques*, Vol. 3, 255–265, 2018.

23. Roth, T. E. and W. C. Chew, "Lorenz gauge potential-based time domain integral equations for analyzing subwavelength penetrable regions," *IEEE Journal on Multiscale and Multiphysics Computational Techniques*, Vol. 6, 24–34, 2021.

24. Yan, S., "A continuous-discontinuous Galerkin method for electromagnetic simulations based on an all-frequency stable formulation," *Progress In Electromagnetics Research M*, Vol. 106, 153–165, 2021.

25. Sharma, S. and P. Triverio, "Electromagnetic modeling of lossy interconnects from DC to high frequencies with a potential-based boundary element formulation," *IEEE Transactions on Microwave Theory and Techniques*, Vol. 70, No. 8, 3847–3861, 2022.

26. Zhang, B., D.-Y. Na, D. Jiao, and W. C. Chew, "An A-Φ formulation solver in electromagnetics based on discrete exterior calculus," *IEEE Journal on Multiscale and Multiphysics Computational Techniques*, Vol. 8, 11–21, 2022.

27. Zhu, Y. and A. C. Cangellaris, *Multigrid Finite Element Methods for Electromagnetic Field Modeling*, Vol. 28, John Wiley & Sons, 2006.

28. Jiang, P., G. Zhao, Q. Zhang, and Z. Guan, "Compatible finite element discretization of generalized Lorenz gauged charge-free a formulation with diagonal lumping in frequency and time domains," *Progress In Electromagnetics Research M*, Vol. 64, 167–179, 2018.

29. Vico, F., M. Ferrando-Bataller, T. B. Jiménez, and D. Sánchez-Escuderos, "A decoupled charge-current formulation for the scattering of homogeneous lossless dielectrics," *2016 10th European Conference on Antennas and Propagation (EuCAP)*, 1–3, IEEE, 2016.

30. Li, J., X. Fu, and B. Shanker, "Decoupled potential integral equations for electromagnetic scattering from dielectric objects," *IEEE Transactions on Antennas and Propagation*, Vol. 67, No. 3, 1729–1739, 2018.

31. Jin, J.-M., *Theory and Computation of Electromagnetic Fields*, John Wiley & Sons, 2011.

32. Stone, M. and P. Goldbart, *Mathematics for Physics: A Guided Tour for Graduate Students*, Cambridge University Press, 2009.

33. Stewart, G. W., "A Krylov-Schur algorithm for large eigenproblems," *SIAM Journal on Matrix Analysis and Applications*, Vol. 23, No. 3, 601–614, 2002.

34. Grote, M. J. and T. Huckle, "Parallel preconditioning with sparse approximate inverses," *SIAM Journal on Scientific Computing*, Vol. 18, No. 3, 838–853, 1997.

35. Pozar, D. M., *Microwave Engineering*, John Wiley & Sons, 2009.